Simulation of Incompressible Flow through Rhombohedric Pores

R. Viola[*1,3], F. Zama[2], M.Tuller[3], E. Mesini[1]
[1]Dept. DICMA, University of Bologna, [2] Dept. of Mathematics, University of Bologna,
[3]Dept. of Soil, Water, and Environmental Science, The Univ. of Arizona, Tucson, AZ
*Corresponding author: rossella.viola@unibo.it , DICMA, V. Terracini 28, 40131 Bologna.

Abstract

Advances in visualization and discretization of pore structures by means of Computed Tomography, and rapidly increasing computational capabilities, allow numerical modeling of pore-scale fluid flow based on the incompressible Navier-Stokes equations rather than using a macroscopic approach based on Darcy's law. Understanding and modeling of pore-scale flow phenomena has wide-ranging implications for petroleum engineering and hydrogeology, specifically for modeling of well-reservoir interactions, coupling of surface and groundwater flows, or flow in fractured porous media.

To test the capabilities of the COMSOL Multiphysics modeling platform, we investigated flows through idealized pore geometries and analyzed the effect of varying pressure gradients on velocity fields. The choice of a rhombohedric cell was motivated by experiments conducted with both uniform sands and glass beads with porosities between the extremes for cubic (48%) and rhombohedral packing of uniform spheres (26%).

Keywords: rhombohedric unit-pore cell, pore-scale Reynolds number, porous media

1. Introduction

Although the Reynolds number (Re) [1-3] is used as a criterion for transition from laminar to turbulent flow in pipe hydraulics, such parameter is difficult to define for complex porous media with intricate pore geometries. If at the macroscopic scale a large number of random, local signals are averaged over a representative elementary volume, information regarding microscopic turbulence is likely to be lost. Antohe and Lage [4] show experimental evidence for microscopic turbulence in a three-dimensional porous medium. In packed beds the representative dimension of the largest flow eddy is limited by the pore dimension that is usually much smaller than the macroscopic dimension of the system. Several authors [5-7] conclude that in packed beds the transition from laminar to turbulent flow is gradual and the critical Re calculated based on average pore dimensions is several times lower than for flow through a straight pipe. For complex porous media, Bear [8] shows that Re values at the onset of turbulence are at least one order of magnitude larger than Re values at which deviation from Darcy's law can be observed, and that caution needs to be exercised to not mistake these values for each other [9].

Microscopic flow patterns in porous media have been analyzed with various techniques, such as laser Doppler anemometry [10], confocal laser scanning microscopy [11, 12], magnetic resonance imaging, dynamic NMR microscopy [13, 14], and direct visualization [5]. The formation of a boundary layer near the solid-liquid interface and subsequent development of an inertial core in the center of pores was interpreted as the reason for deviations from the linear relationship between pressure drop and flow rate. The influence of flow rate on the pore-scale pattern was also studied by means of magnetic resonance imaging [15]. Visualization of fluid velocity distributions within pores of a bed of 5-mm diameter glass beads revealed that for increasing effective (macroscopic) Reynolds numbers velocity profiles in individual pores became flatter at the center, and steeper close to the solid-liquid interface [16]. Regions with countercurrent flow were also found within the laminar flow regime.

Only a few studies focused on three-dimensional (3-D) eddies at the pore-scale. Cardenas [17] applied finite-element simulations to analyze vortices and solute distributions in a single pore throat between cubic-packed spherical and ellipsoidal grains (1–2 mm diameter). Results of this study reveal proportionality between discharge and imposed pressure gradients up to Reynolds numbers of about 3. A significant contrast in Peclet number, very small within vortices (<1), and large within the bulk flow (>10,000) outside the dead zone, caused tailing of the solute plume.

In this paper we investigate flow through rhombohedric unit pore cells and apply finite element simulations in conjunction with incompressible Navier-Stokes equations to analyze effects of pore geometry on flow behavior, taking into account both water and oil as permeating fluids. We illustrate streamlines and velocity fields at different pressure gradients and point out existence of preferential flow paths, both in one and two joint rhombohedric cells. To quantitavely define flow patterns within rhombohedric pore space, we relate Re and pressure gradient to velocity.

2. Methods

Numerical simulations were conducted by first considering the case of laminar flow (low Re < 3), and water as permeating fluid. The three-dimensional incompressible Navier-Stokes equations were applied to a single pore throat between rhombohedric-packed grains (1.9-mm diameter) (Fig. 1).

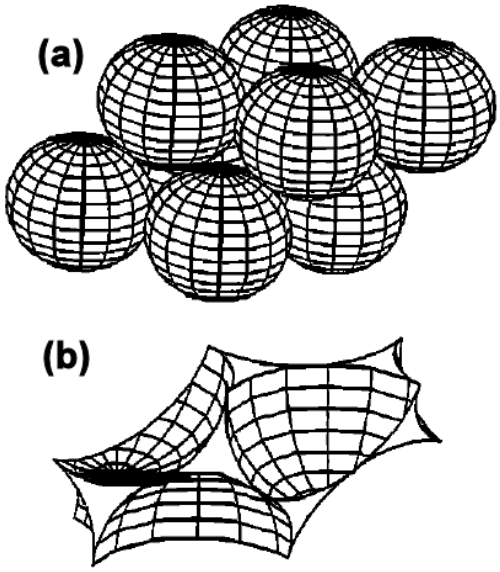

Fig.1: (a) Rhombohedral packing of identical spheres, and (b) unit pore cell (modified from Gvirtzman and Roberts [18]).

Steady incompressible flow through a pore can be defined by the Navier-Stokes equations:

$$\rho(u\,.\nabla)u + \nabla p = \mu\nabla^2 \mathrm{u},$$
$$\nabla . u = 0$$

where ρ is fluid density (1000 kg m^{-3}), u=[u,v,w] is the velocity vector, μ is the dynamic viscosity (μ = 0.001 Pa s), and p is the total pressure. To avoid highly skewed mesh elements, the unit cell was constructed with 0.1 mm spaces between individual grains at their closest points.

The following boundary conditions were used for the simulations.

(a) Wall no-slip conditions (u=0) at the grains surfaces.

(b) Slip symmetry at the interfaces between different rhombohedric cells.

(c) The inlet surface is defined on the (x,y) plane at z=0.

Pressure boundary conditions were used together with a Dirichlet condition ($p = p_0$) assigned at the inlet surface. The condition of no viscous stress was added to assure stability in case of low Reynolds numbers.

$$(\eta(\nabla \boldsymbol{u} + (\nabla \boldsymbol{u})^T)\boldsymbol{n} = 0).$$

(d) The outflow surface is defined at z=1.E-3 on the (x,y) plane. For this case a homogeneous pressure condition was assigned (p=0).

The COMSOL Multiphysics platform was used for simulations. The geometry of the computational domain was defined with the 3-D graphical tool set in the Comsol Multiphysics graphical interface. Eight spheres with 0.95-mm radius were constructed and aligned in rhombohedric fashion. After scaling the axis to 1.E-3, six planes were embedded forming a solid geometry. The spheres were then subtracted to obtain a unit pore cell as shown in Fig.1b.

The finite-element solution was computed for meshes with 1.5E+5 to 5.0E+5 tetrahedral elements. Lagrange p_2-p_1 elements were used in all simulations and streamline diffusion (Galerkin least-squares) was applied to assure stability. The complexity of the numerical problem, expressed in terms of degrees of freedom (DOF), is in the range of [1.E+5, 4.E+5] elements. The Parallel Direct Solver (PARDISO) was used for small dimension problems otherwise the iterative BiCGstab solver coupled with geometric multigrid was applied. In most cases between 4 and 8 iteration steps were required with the non linear solver for the solution to converge. A 4-processor workstation with 16 GB of shared RAM was used for computations. Computation times ranged from about 5 minutes to 1 hour.

3. Results

Streamline analysis and the behaviour of velocity fields and pressure gradients at different pore-scale Re provide evidence for the existence of preferred flow paths within the unit cell. This is shown for both water and oil as saturating fluids.

3.1 Streamlines and Velocity Fields

First we visualized streamlines within 3-D velocity fields for different pressure gradients. Figure 2 shows streamlines calculated for inlet pressures of 1 Pa (Fig.2a) and 5 Pa (Fig.2b) at the bottom face and zero pressure boundary at all outlet faces. For 1 Pa pressure difference (Fig.2a) highest velocities can be observed close to grain surfaces, while flow velocities between spheres that are separated by 0.1 mm at their closest point remain relatively low.

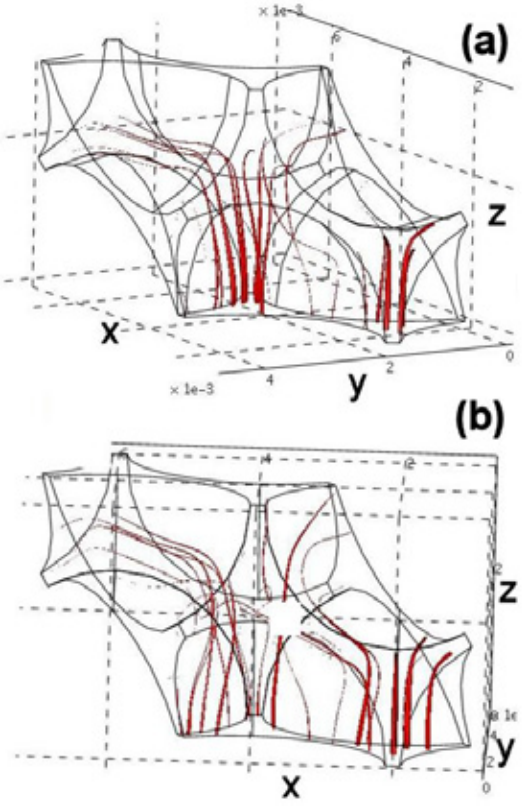

Fig.2: Rhombohedric unit pore cell. (a) Streamlines for 1 Pa inlet pressure at the bottom and zero pressure boundary at outlet faces. (b) Streamlines for 5 Pa inlet pressure at the bottom and zero pressure boundary at outlet faces.

It is apparent from Figure 2b that for higher pressure gradients streamlines reach more distant regions, hence highest velocities occur further away from the solid pore walls.

Although streamlines seem to be more uniformly distributed when the gradient is higher (Fig.2b), for both cases we see evidence of preferred flow paths on the left side of the cell. This is due to the rhombohedric geometry of the pore space with more accessible volume towards the left (path of least resistance). Abrupt changes of flow directions (i.e. streamline distortion) indicate that Darcy's law is not applicable.

3.2 Pore-Scale Reynolds Number and Velocity Fields

In order to quantitatively define flow patterns and to confirm different velocity values at the outlet faces, a pore-scale Re was considered. Figure 3 shows two of the outlet faces obtained for inlet pressures of 1 Pa and Re=10 (Figs3a,b) and 5 Pa and Re=50 (Fig.3c,d). The faces in (a) and (c) are parallel to the inlet face, whereas the faces in (b) and (d) are located on the right side.

The boundary layer near the solid-liquid interface and the development of an inertial core in the center of the pore is visible only on one side of the outlet faces, indicating preferred flow in one direction. For higher Re, the velocity field shows onset of fluid invasion to adjacent regions, involving the 'pore-neck' and reaching the lateral face with higher velocity at the wall. The maximum velocity values for 1 and 5 Pa are 0.04 m/s and 0.2 m/s, respectively. There is proportionality between pressure gradient and velocity.

To further investigate the existence of preferred flow paths, simulations have been performed for two joint rhombohedric cells. Even for this case, velocity remains zero just on one side of the outlet face (Fig.4).

3.3 Pressure Gradients

Next we looked at the pressure gradient perpendicular to the inlet face (z-direction). Results for Re of 10 (Fig.5a,b) and 50 (Fig.5c,d) are presented. Inlet faces are shown in (a) and (c); outlet faces are depicted in (b) and (d).

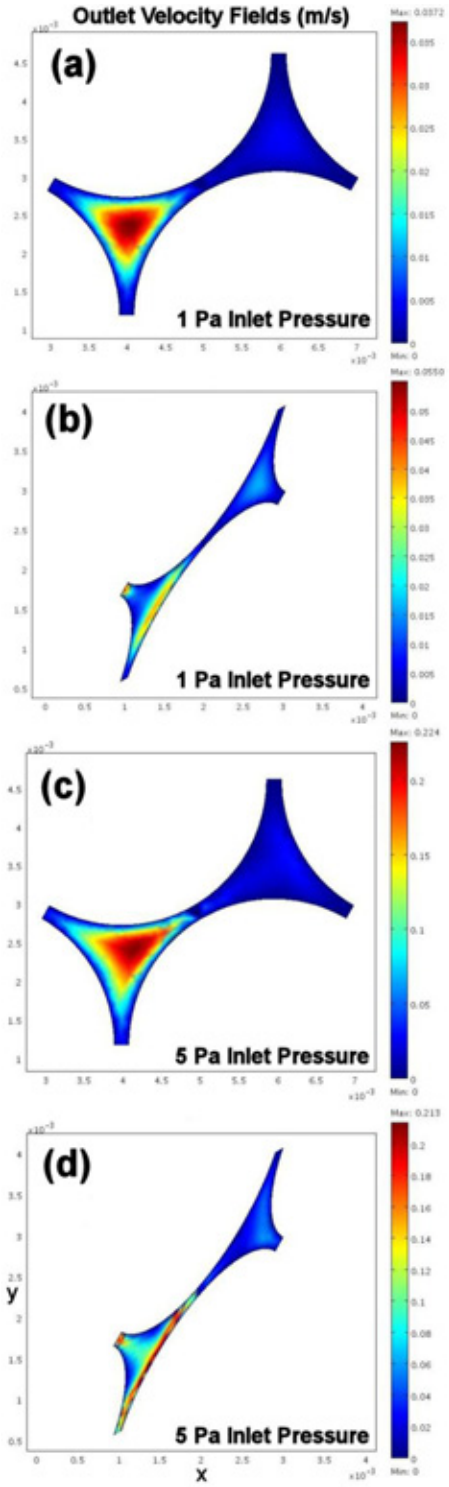

Fig.3: (a,b) Outlet faces for inlet pressures of 1 Pa and Re=10 and (c,d) 5 Pa and Re=50. The faces in (a) and (c) are parallel to the inlet face, whereas the faces in (b) and (d) are located on the right side.

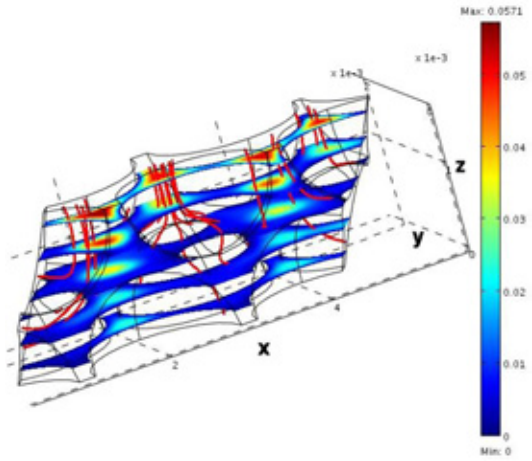

Fig.4: Two joint rhombohedric cells with the inlet face on top.

For Re=10 the highest pressure gradient at the inlet face is about one order of magnitude higher than at the outlet face (from 2000 to 100 N/m^3) (Fig.5a,b). For Re=50 the difference spans over several orders of magnitude, and the pressure gradient at the outlet is much higher (from -5000 to 4000 N/m^3). Highest gradients are concentrated on the right side of the outlet face for Re=10 (Fig.5b), whereas for Re=50 regions with high gradients are also visible close to the pore walls on the left side (Fig.5d).

From velocity profiles depicted in Figure 3 it is apparent that in both cases the constant pressure regions on the right side of the outlets are associated with zero velocities.

3.4 Comparison of Different Fluids

To look at different fluids we conducted a second set of simulations for oil assuming a dynamic viscosity of 0.01 Pa s and a density of about 800 kg m^{-3}.

Figure 6 shows streamlines and velocity fields obtained for different inlet pressures (5, 10, and 100 Pa). It is apparent from Fig.6a that for low pressure gradients, velocities observed at the outlet faces are below the values observed for water (Fig.3). In addition, streamlines are more uniformly distributed and never overlap, even for gradients of 100 Pa (Fig.6c), indicating laminar flow conditions.

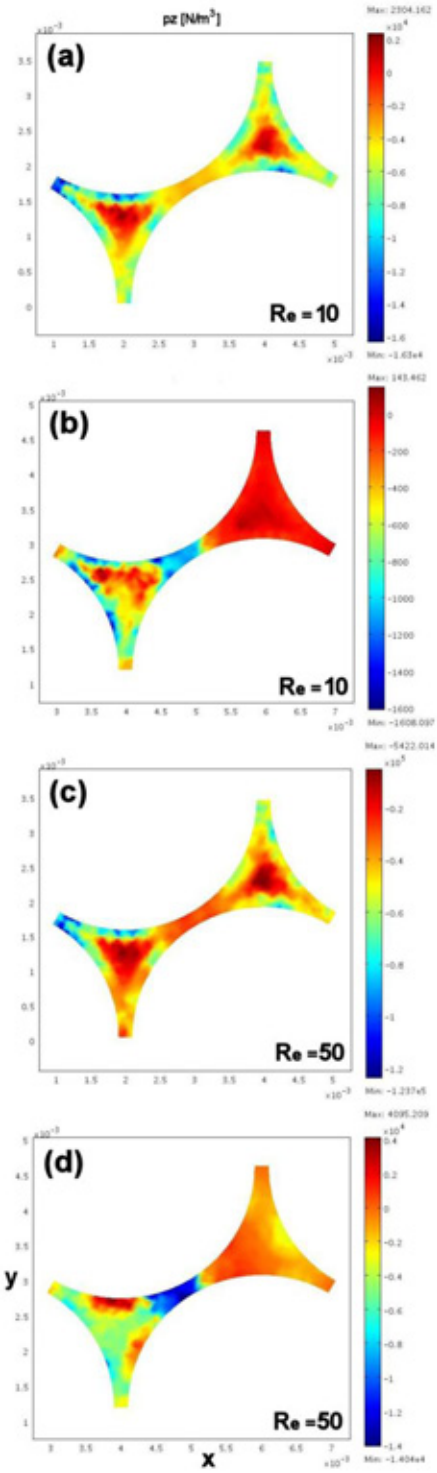

Fig.5: Pressure gradients perpendicular to the inlet face (z-direction). (a,b) Results for Re=10 and (d,c) Re=50 are presented. Inlet faces are shown in (a) and (c); outlet faces are depicted in (b) and (d).

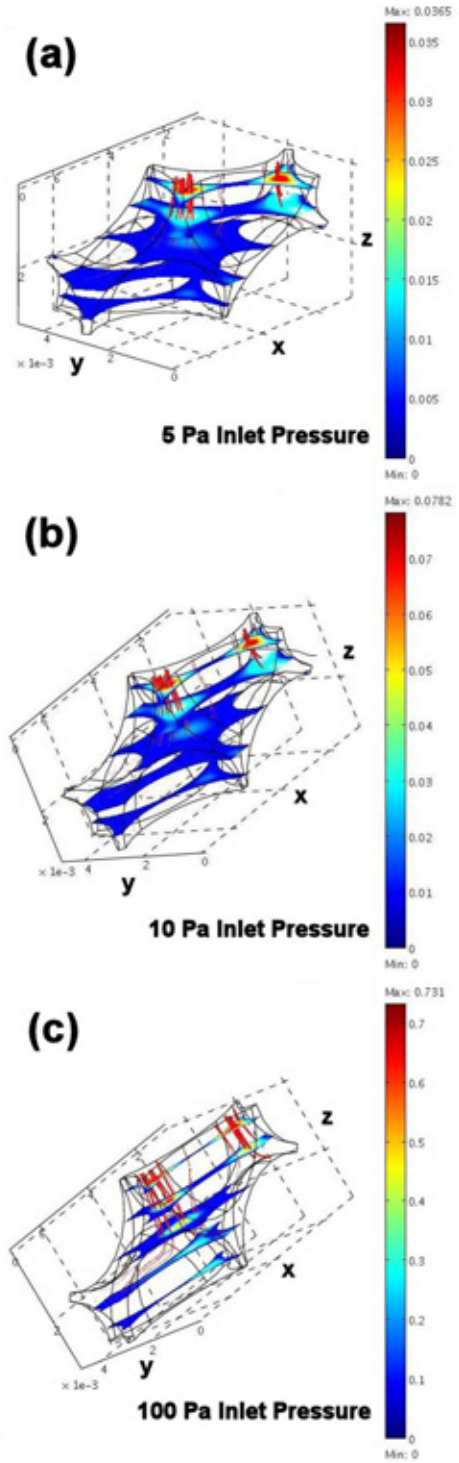

Fig.6: Streamlines and velocity fields for oil, with pressure gradients of (a) 5 Pa, (b) 10 Pa, and (c) 100 Pa.

4. Conclusions

Incompressible Navier-Stokes equations were applied to simulate flow through idealized rhombohedric pores with the COMSOL NS incompressible fluid flow module. Effects of varying pressure gradients on velocity fields were analyzed. Results show proportionality between gradients and velocities for pore-scale Reynolds numbers ranging from 10 to 50, indicating laminar flow behavior.

Presented visualizations of streamlines and velocity fields show preferred flow paths within rhombohedric pores. The presence of a boundary layer near the solid-liquid interface and the development of an inertial core in the center of the pore are visible only on one side of the outlet face. In addition, higher velocity (higher Re) is confirmed when the pore-neck and the lateral faces are reached.

While for all simulated cases apparent streamline distortion points to inapplicability of Darcy's law, application of incompressible Navier-Stokes equations seems to realistically represent flow phenomena in idealized pore space.

5. References

[1] O. Reynolds, An Experimental Investigation of the Circumstances Which Determine Whether the Motion of Water Shall Be Direct or Sinuous, and of the Law of Resistance in Parallel Channels, *Philos. Trans. R. Soc. Lond*. **174**, 935-982, 1883.

[2] H.T. Barnes, E.G. Coker, The Flow of Water through Pipes.--Experiments on Stream-Line Motion and the Measurement of Critical Velocity, *Proc. R. Soc. Lond*. **74**, 341-356, 1904.

[3] W. Pfenninger, Transition experiments in the inlet length of tubes at high Reynolds numbers. in: G.V. Lachmann (Ed.), *Boundary Layer and Flow Control*, vol. **2**, Pergamon Press, New York, 970–980, 1961.

[4] B.V. Antohe, J.L. Lage, A General Two-Equation Macroscopic Turbulence Model for Incompressible Flow in Porous Media, *Int. J. Heat Mass Transfer* **40**, 3013-3024, 1997.

[5] T.H. Wegner, A.J. Karabelas, T.J. Hanratty, Visual studies of flow in a regular array of spheres, *Chem. Eng. Sci.* **26** , 59-63, 1971.

[6] I.F. Macdonald, M.S. El-Sayed, K. Mow, F.A.L. Dullien, Flow through porous media - the Ergun equation revisited, Ind. Eng. Chem. Fundam. **18**, 199-208, 1979.

[7] D. Seguin, A. Montillet, J. Comiti, F. Huet, Experimental characterization of flow regimes in various porous media II: transition to turbulent regime. *Chem. Eng. Sci.* **53**, 3897-3909,1998.

[8] J. Bear, *Dynamics of Fluids in Porous Media*, 181–182, Dover Publications, New York, 1988.

[9] F.A.L. Dullien, *Porous Media: Fluid Transport and Pore Structure*, Academic Press, San Diego, 1992.

[10] A.R. Yevseyev, V.E. Nakoriakov, N.N. Romanov, Experimental investigation of a turbulent filtrational flow, *Int. J. Multiphase Flow* **17**,1, 103-118, 1991.

[11] U. Tallarek, E. Rapp, H. Sann, U. Reichl, A. Seidel-Morgenstern, Quantitative study of electrokinetic transport in porous media by confocal laser scanning microscopy, *Langmuir* **19**, 4527-4531, 2003.

[12] F.C. Leinweber, U. Tallarek, Concentration polarization-based nonlinear electrokinetics in porous media: induced-charge electroosmosis, *J. Phys. Chem. B*, **109**, 21481-21485, 2005.

[13] M.D. Shattuck, R.P. Behringer, G.A. Johnson, J.G. Geordiadis, Onset and stability of convection in porous media: Visualization by magnetic resonance imaging, *Phys. Rev. Lett.* **75**, 1934-1937, 1995.

[14] J.D. Seymour, P.T. Callaghan, A generalized approach to the measurement of flow and dispersion in a porous medium using nuclear magnetic resonance, *AIChE J.* **43** , 2096-2111, 1997.

[15] M.L. Johns, A.J. Sederman, A.S. Bramley, L.F. Gladden, P. Alexander, Local transitions in flow phenomena through packed beds identified by MRI, *AIChE J.* **46**, 2151-2161, 2000.

[16] Y.E. Kutsovsky, L.E. Scriven, H.T. Davis, B.E. Hammer, NMR imaging of velocity profiles and velocity distributions in bead packs *Phys. Fluids* **8** , 863-871, 1996.

[17] Cardenas M.B., Three dimensional vortices in single pores and their effect on transport. *Geophys. Res. Lett.*, **35**, 1-6, 2008.

[18] Gvirtzman, H. and Roberts, P.V., Pore scale spatial analysis of two immiscible fluids in porous media. *Water. Resour. Res*, vol. **27**, no. 6, 1165-1176, 1991.